Rayleigh-wave group velocity tomography using traffic noise at Long Beach, CA

Jason P. Chang and Biondo Biondi

ABSTRACT

Anthropogenic sources recorded by passive seismic arrays provide the opportunity for ambient noise cross-correlation techniques to effectively use frequencies well beyond the microseism band. Using data recorded by a dense array in Long Beach, California, we demonstrate that high-frequency (> 3 Hz) fundamental- and first-order-mode Rayleigh waves generated by traffic noise can be extracted from the ambient noise field and used for tomographic studies. Here, we use travel times of the fundamental-mode Rayleigh waves in a straight-ray tomography procedure to derive group velocity maps at 3.00 Hz and 3.50 Hz. The velocity trends in our results correspond to shallow depths and correlate well with lithologies outlined in a geologic map of the survey region. As expected, less-consolidated materials display relatively low velocities, while more-consolidated materials display relatively high velocities. Our results suggest important implications for research investigations concerned with the near-surface.

INTRODUCTION

Extracting surface waves from the ambient noise field for use in tomographic studies is well-established at both regional and continental scales (e.g., Shapiro et al., 2005; Yang et al., 2008; Bensen et al., 2008). The success of these studies has encouraged recent investigation of this technique at the exploration scale. In ocean-bottom environments, de Ridder et al. (2014) and Mordret et al. (2014) obtained reliable time-lapse group and phase velocity maps, respectively, of the Valhall overburden, while de Ridder et al. (2015) recovered phase velocity and anisotropy maps representative of subsidence patterns at Ekofisk. In those cases, they examined frequencies in the microseism band (< 2 Hz). In land environments, passive seismic arrays of sufficient density, size, and duration for these sorts of studies are rare.

One array that does meet these requirements was located in Long Beach, California (map in Figure 1). Deployed in January 2012 by NodalSeismic, the array spans an 8.5×4 km^2 region and consists of approximately 2400 vertical-component geophones. With an average geophone spacing of 100 m and a continuous 3-month recording period, the array is well-suited for exploration-scale tomography using ambient noise. Dahlke et al. (2014) were able to create phase velocity maps at low frequencies (approximately 1 Hz) that resolved the location of the Newport-Inglewood Fault. At the

neighboring array, Lin et al. (2013) were able to create similar Rayleigh-wave phase velocity maps for frequencies up to 2 Hz that successfully imaged the same fault.

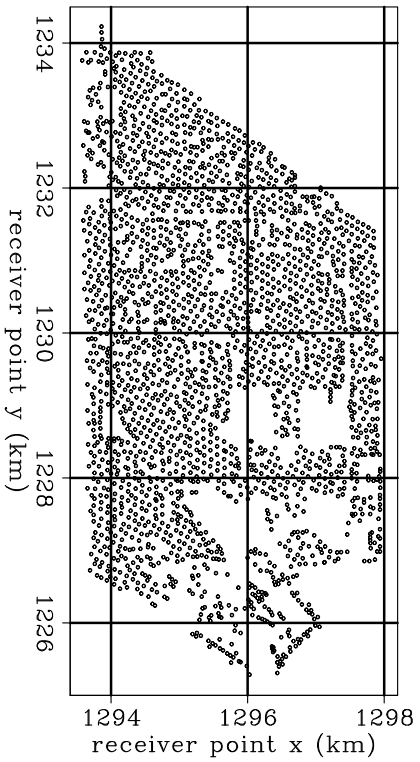

Figure 1: Map of stations at the Long Beach passive seismic array. Coordinates are NAD27, CA State Plane, Zone 7, kilometers. [**CR**]

The focus of our present study is to create high-frequency (> 3 Hz) group velocity maps at the Long Beach array using passive seismic recordings. At these frequencies, traffic noise dominates the ambient noise field. Power spectral density maps (Chang et al., 2013; Nakata et al., 2015) and beamforming of the ambient noise field (Chang et al., 2014) reveal Interstate 405 as the dominant source of seismic energy and local roads as the secondary source. We begin with an overview of our ambient noise processing procedure for harnessing this traffic noise. We then explain our fundamental-mode Rayleigh-wave travel time selection process and straight-ray tomography approach. To validate our results, we compare our group velocity maps to a geologic map of the region. Finally, we examine the resolution of our results with checkerboard tests.

ESTIMATING GREEN'S FUNCTIONS

To extract inter-station Green's functions from ambient noise recordings, we apply a processing procedure adapted from Bensen et al. (2007). Continuous recordings from all receiver pairs are divided into simultaneous, non-overlapping two-hour time windows. To compensate for expected variations in the source amplitude due to varying traffic conditions over time, we whiten the traces prior to cross-correlation.

In the frequency domain, this process is expressed as:

$$[G(x_B, x_A, \omega) + G^*(x_B, x_A, \omega)] = \left\langle \left(\frac{U(x_B, \omega)}{\{|U(x_B, \omega)|\}} \right) \left(\frac{U^*(x_A, \omega)}{\{|U(x_A, \omega)|\}} \right) \right\rangle, \quad (1)$$

where G is the Green's function between two receiver locations (x_A, x_B), $U(x, \omega)$ is the spectrum of the wavefield at a given receiver location x, $*$ is the complex conjugate, $\langle \cdot \rangle$ is the time-averaged ensemble, $|\cdot|$ is the magnitude of the spectrum, and $\{\cdot\}$ is a 0.003 Hz running window average used for normalizing the signal. This procedure is equivalent to calculating the cross-coherence between two traces. For this study, we sum 384 two-hour time windows (or 32-days worth) of cross-correlations.

Applying this processing procedure to a line of receivers running perpendicular to Interstate 405, Chang et al. (2014) verified that the extracted Green's functions above 3 Hz were dominated by fundamental- and first-order-mode Rayleigh waves generated by the highway and local roads. An example of an extracted Green's function with two Rayleigh-wave modes is shown in Figure 2. In this study, we use these correlations to perform group velocity tomography.

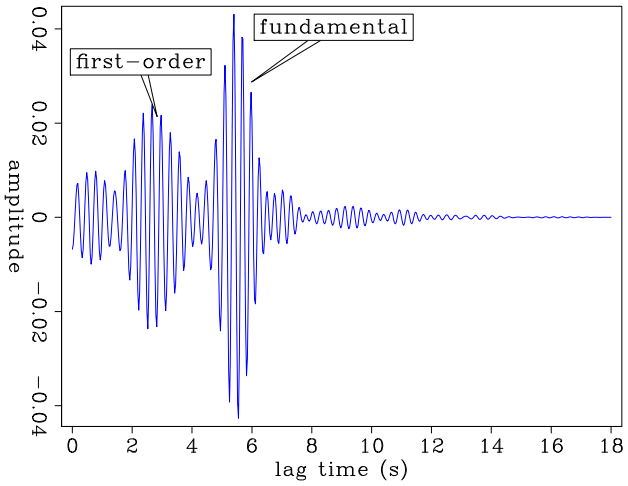

Figure 2: Example of an estimated Green's function between a virtual source and receiver at 3.50 Hz. The earlier peak corresponds to the first-order Rayleigh-wave mode, while the later peak corresponds to the fundamental mode. [**CR**]

GROUP VELOCITY TOMOGRAPHY

Travel time selection

Group travel time between two stations is picked as the peak of the envelope of the bandpass-filtered trace that has been folded over zero time lag. In the frequency domain, the filter is applied as a Gaussian taper centered at the frequency of interest. For this study, we are interested in shallow velocity trends. Because the fundamental-mode Rayleigh wave is more sensitive to shallower depths than the first-order mode (for a given frequency), we are only interested in travel times of the fundamental mode. For this process, we calculate two linear moveout windows: one based on the fundamental mode, and the other based on the first-order mode. Both windows are

between 2 and 3 seconds wide for the frequencies examined. Respective velocities are estimated from the frequency-wavenumber representation of a virtual source gather centered on Interstate 405 and sorted by radial offset (Figure 3). We first apply a mute to the moveout window associated with the first-order mode. This is done for two reasons. One is to avoid accidentally associating this earlier peak with the travel time of the fundamental mode. Another is to avoid bias in our signal-to-noise ratio (SNR) estimate due to the presence of multiple distinct peaks. Here, we calculate SNR as the ratio of the maximum amplitude of the envelope inside the fundamental-mode moveout window to the root-mean-square of the envelope outside both the fundamental and first-order moveout windows.

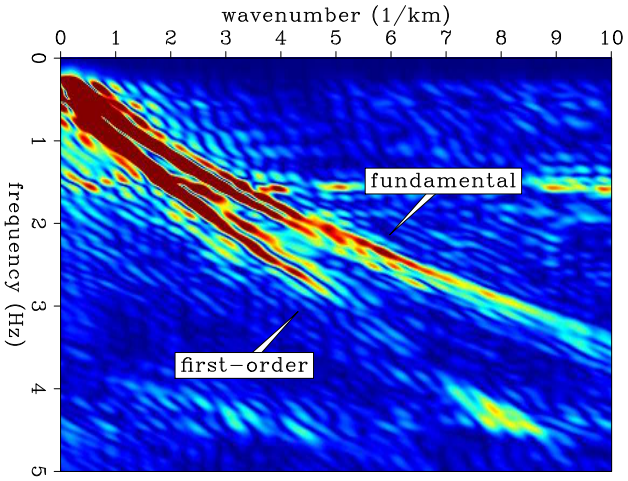

Figure 3: Frequency-wavenumber plot derived from a virtual source gather centered at Interstate 405. Note the two clear Rayleigh wave modes. The shallower sloping event corresponds to the fundamental mode, while the steeper sloping event corresponds to the first-order mode. [**CR**]

For the two central frequencies we examined (3.00 Hz and 3.50 Hz), we kept correlations with SNR greater than 5. Figure 4 shows maps of travel times obtained from traces at 3.50 Hz that have passed the SNR criterion for four different virtual source locations. Because Interstate 405 effectively serves as an active source, it causes artificially early peaks in the correlations where the virtual source and receiver are on opposite sides of the highway. These earlier-than-expected peaks degrade the SNR and lead to the lack of accepted travel times on the opposite side of Interstate 405. We can see this effect in Figures 4(a) and 4(b). In the former figure, the virtual source is located north of the highway, and the truncated border of the travel time map toward the south correlates well with the path of the highway. A similar pattern is observed in the latter figure, where the virtual source is located south of the highway. Further away from the highway, the ambient noise field is dominated by Rayleigh waves generated by local traffic (Chang et al., 2014). Thus, it is no surprise that we still have suitable travel times when the virtual source is in the center of the array (Figure 4(c)). In the sparse southeast part of the array, there are relatively few sources of traffic noise due to the lack of busy roads and the presence of a marina. Thus, it is expected that there are very few suitable travel times in that part of the array (Figure 4(d)). Together, these travel time maps suggest that our fundamental-mode Rayleigh-wave travel time selection process is potentially reliable.

For our tomography study, we only use correlations with virtual source-receiver

spacing between 0.5 and 1.7 km at 3.00 Hz and between 0.4 and 1.5 km at 3.50 Hz. The minimum spacing is approximately one wavelength longer than the suggested minimum of three wavelengths (Moschetti et al., 2007). The maximum spacing is chosen by looking at the travel time maps. Out of a possible $2,980,143$ traces, we kept $530,876$ traces (18%) at 3.00 Hz and $403,523$ traces (13%) at 3.50 Hz. Although we used significantly fewer traces than available, the inversion problem remains highly over-determined. The goal is to use the most reliable travel times, not the most number of travel times.

Inversion procedure

To obtain group velocity maps, we employ a straight-ray tomography procedure with regularization. The problem is posed as solving for the slowness perturbation, $\Delta\mathbf{m}$, with respect to an average slowness m_0. Therefore, the final slowness model, $\mathbf{m}$, is defined as $\mathbf{m} = \mathrm{m}_0 + \Delta\mathbf{m}$. The average slowness is calculated from the travel time and offset information of all traces that pass quality control. We subtract the contribution of the average slowness from each travel time to obtain residual travel times, $\Delta\mathbf{t}$.

Modeled residual travel times are obtained by applying a straight-ray tomography operator, $\mathbf{F}$, to a slowness perturbation model. Rows of the operator contain the length of a straight ray through each model grid cell for a single virtual source-receiver path. For this data set, we construct a 110×220 model grid space, with each grid covering a 50×50 m^2 region. We use a conjugate gradient approach to minimize the following objective function:

$$J(\Delta\mathbf{m}) = ||\mathbf{F}\Delta\mathbf{m} - \Delta\mathbf{t}||_2^2 + \epsilon||\nabla^2\Delta\mathbf{m}||_2^2 \quad . \tag{2}$$

∇^2 represents the Laplace operator, which is the roughening operator used for regularization. ϵ represents regularization strength, which balances the data-fitting objective and the model-smoothing objective. We iterated 25 times, which is enough to converge to a solution (Figure 5).

Model selection

To choose the regularization strength (and hence a model), we examine the L-curve (Aster et al., 2013). An L-curve is a trade-off curve between the data residual misfit ($||\mathbf{Fm}-\mathbf{d}||_2$) and the model semi-norm ($||\nabla^2\mathbf{m}||_2$). Different regularization strengths will plot different points on this graph, with lower values sitting at the top left of the curve and higher values sitting at the bottom right of the curve. The resulting curve shape is typically an "L". Often, the ϵ that produces a solution closest to the corner of this curve is chosen, as it balances the model smoothing and data fitting parameters best.

For these tomography problems, we examine ϵ values from 0 to 5, in increments of 0.25. The resulting L-curves for 3.00 and 3.50 Hz are shown in Figures 6(a) and 6(b),

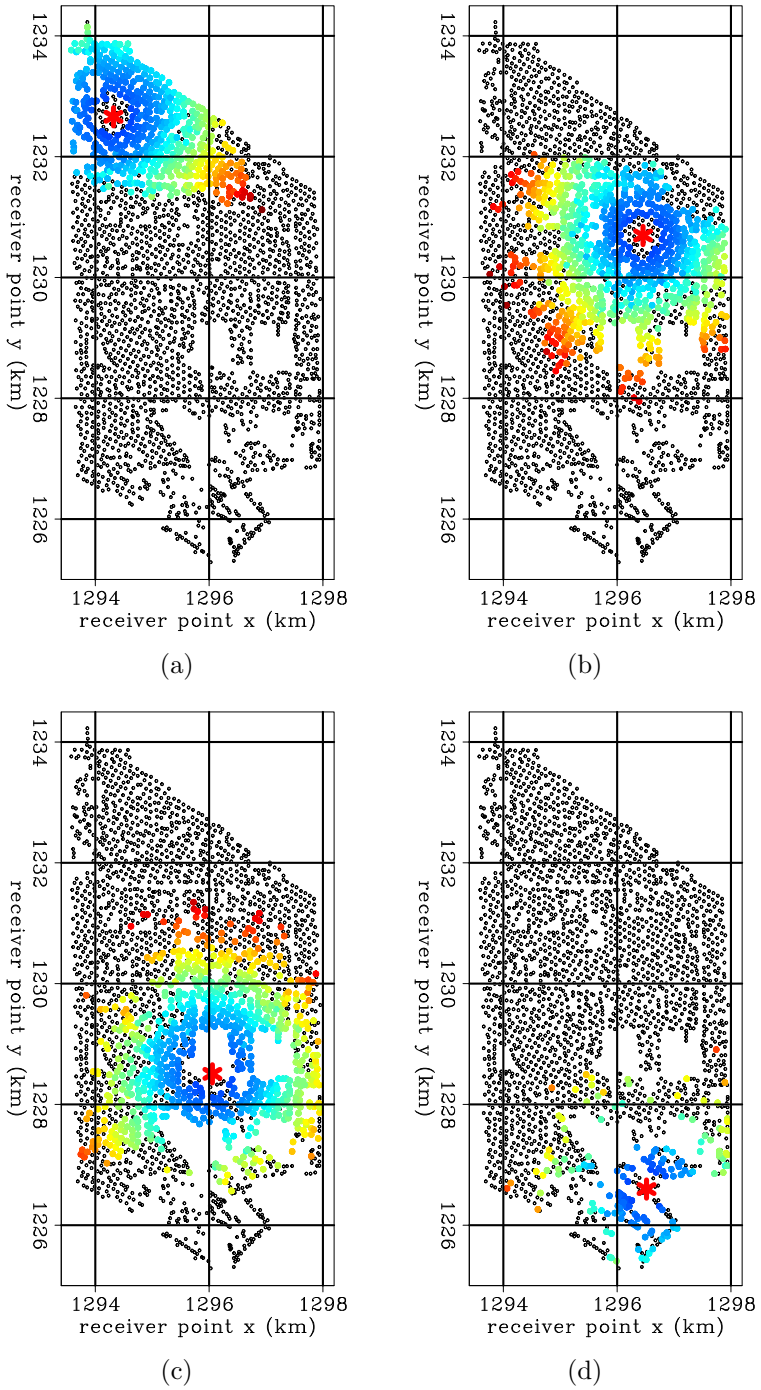

Figure 4: Fundamental-mode Rayleigh-wave travel time maps at 3.50 Hz for four different virtual source locations (indicated by red asterisks). Warmer colors correspond to later travel times. Only travel times obtained from correlations with SNR greater than 5 are displayed. (a) Virtual source north of Interstate 405. (b) Virtual source south of Interstate 405. In these cases, note the lack of suitable travel times on the other side of the highway. (c) Virtual source near the center of the array. (d) Virtual source near the coastline. The relative lack of suitable travel times in the southeast region of the array is likely due to the relative lack of traffic noise. [**CR**]

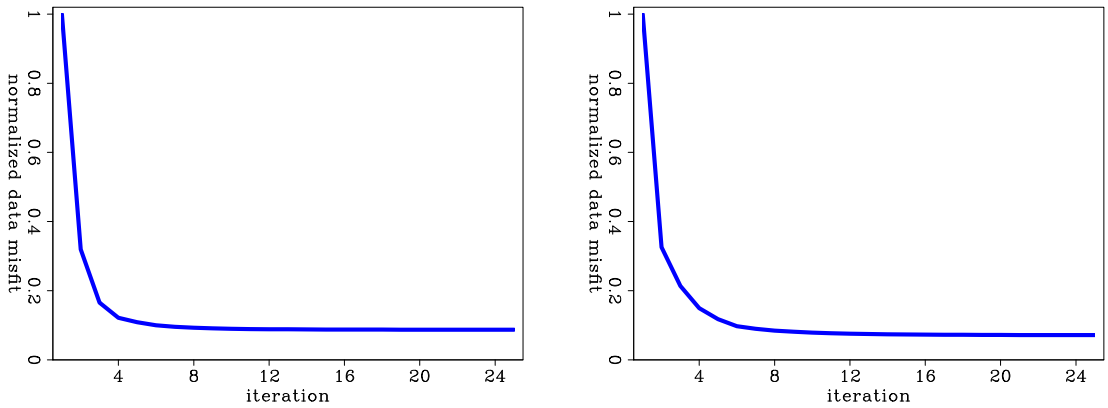

(a) (b)

Figure 5: Norm of the data residual as a function of iteration. Residuals are normalized by the initial residual. (a) 3.00 Hz. (b) 3.50 Hz. [**CR**]

respectively. To better locate the corner point, we plot the axes on a logarithmic scale. In both cases, we choose a regularization strength of 1.50 (indicated by the red dots on the curves).

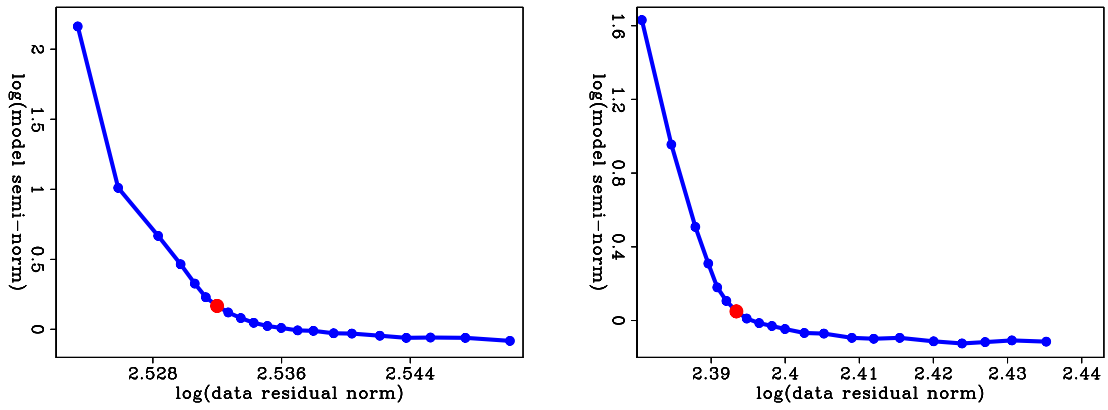

(a) (b)

Figure 6: Trade-off curves between the norm of the data residual and the semi-norm of the resulting model for different regularization strengths ϵ (0 is at the top left of the curve and 5 is at the bottom right of the curve). (a) For 3.00 Hz. (b) For 3.50 Hz. The red dot corresponds to $\epsilon = 1.50$ and is used for the velocity maps shown in this paper. [**CR**]

GROUP VELOCITY MAPS

Due to the dispersive nature of Rayleigh waves, the group velocity map at 3.00 Hz (Figure 7(a)) shows generally higher velocities than those in the group velocity map at 3.50 Hz (Figure 7(b)). However, because the wavelengths at these two frequencies

are similar, it is not a surprise that they show the same general velocity trends and features. We interpret our results with the guidance of a geologic map of the survey region in Figure 7(c) (California Department of Conservation, 2012).

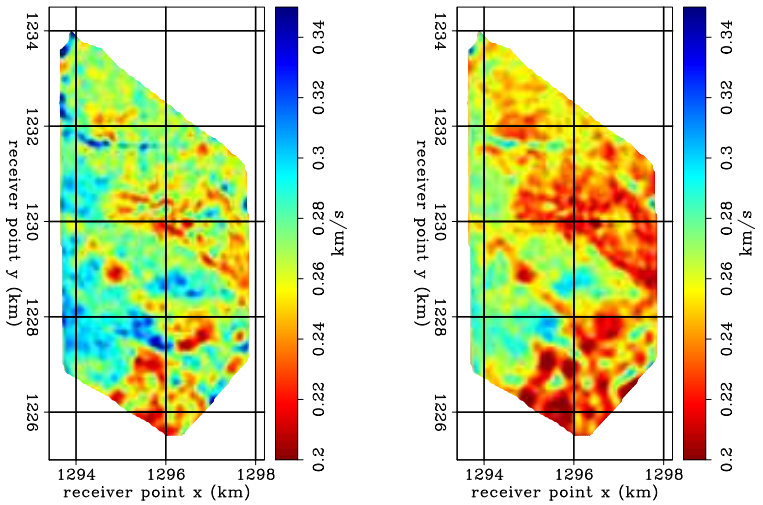

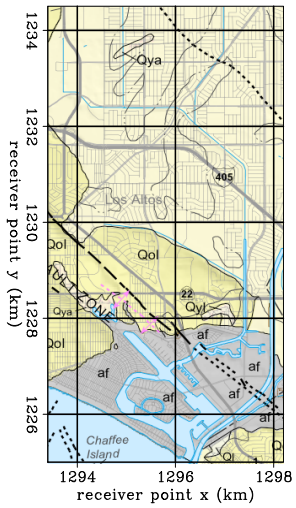

Figure 7: Group velocity maps generated at (a) 3.00 Hz and (b) 3.50 Hz. (c) Geologic map of the survey region (California Department of Conservation, 2012). Note the similarities between the velocity trends in the tomography results and the lithologies outlined in the geologic map. [**CR**] [**CR**] [**NR**]

One of the most prominent trends in our group velocity maps is a boundary cutting northwest-southeast across the array that separates a lower velocity region (north) from a higher-velocity region (south); it is most distinct south of the eastern portion of Interstate 405. The location of this boundary matches well with a boundary in the geologic map that separates Holocene to late Pleistocene alluvial valley deposits (north; light yellow) from late to middle Pleistocene lacustrine, playa, and estuarine

deposits (south; deep yellow). The deposits in the north typically consist of unconsolidated to slightly consolidated material, while the deposits in the south typically consist of slightly to moderately consolidated material. Thus, it is no surprise that we find the northern region to be of a lower velocity than the southern region. Another prominent feature is a low velocity zone in the southeast region of the array. This zone corresponds to the location of Alamitos Bay, which is built on artificial fill (grey region in Figure 7(c)). Thus, our tomography results appear reliable, since artificial fill typically displays relatively low velocities (Wills and Silva, 1998).

Two other features are the high velocities overlaying Interstate 405 and the low velocities overlaying the Newport-Inglewood Fault. The former trend could be an artifact, as travel times from ray paths that cross the highway can be artificially early due to the highway acting as an active source. The latter trend is curious, as the fault displays relatively high velocities at low frequencies and deeper depths (Dahlke et al., 2014; Lin et al., 2013), whereas the fault seems to display relatively low velocities at higher frequencies and shallower depths. We require better understanding of fault systems to determine whether this low-velocity fault trend is reasonable.

MODEL RESOLUTION

We address the spatial resolution of the model in two ways. First, we examine the cumulative ray length in each model grid cell (Figure 8) when using acceptable travel times at 3.50 Hz. Longer ray lengths correspond to more rays passing through the cell. As expected, the ray coverage is highest in the center of the array. The relatively low-coverage areas correspond to gaps in the array. The lack of coverage is particularly evident in the southeast region of the array, where the effect of the lack of receivers is compounded by the relative lack of traffic noise.

Second, we run checkerboard tests. Although there are shortcomings when using this method to assess spatial resolution (Lévěque et al., 1993), we use it here for qualitative purposes. For this procedure, we first add a sinusoidal, or checkerboard, velocity perturbation to our final inverted model. For our study, we examine two checker sizes: 500 m $\times$500 m (Figure 9(a)) and 250 m $\times$250 m (Figure 10(a)). Peaks of the perturbation are set to $\pm$15% of the modeled velocity, which is smaller than the maximum percent difference between the major low- and high-velocity regions. As a result, the actual pattern is not uniform over the model. We then use our forward tomography operator to generate synthetic travel times between virtual source-receiver pairs for the perturbed velocity model. To simulate noise in our actual travel time picks, we add random travel time error to each synthetic travel time based on a Gaussian distribution with a mean of 0 and a standard deviation of 14% of the travel time. This standard deviation is calculated by taking the root-mean-square (RMS) of the absolute differences between each observed travel time and the corresponding synthesized travel time from the final velocity model, normalized by the observed travel time ($|t_{\text{obs}} - t_{\text{syn}}|/t_{\text{obs}}$). It is 14% for both velocity models. Finally, we invert these noisy synthetic travel times using the same parameters we used when inverting

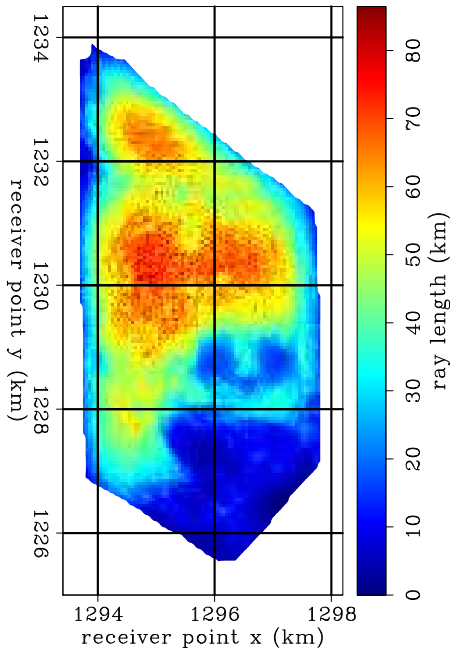

Figure 8: Cumulative ray length map for all station pairs used at 3.50 Hz. Although ray lengths in the southeast part of the array are relatively short, there is still enough coverage to trust the general low-velocity trend. [**CR**]

the actual data.

The inverted results for the larger checkers (500 m ×500 m) and smaller checkers (250 m ×250 m) are shown in Figures 9 and 10, respectively, for both 3.00 Hz and 3.50 Hz. For both checker sizes and both frequencies, it is clear that the high amount of noise in the travel times affects the smoothness of the recovered checkerboard pattern. This suggests we cannot completely trust the absolute velocity in every grid cell of our group velocity maps. Despite this, the overall checkerboard pattern is resolved to a reasonable degree in all cases. For larger checkers, the pattern is resolved throughout nearly the entire array. The exception is the southeast region of the array, where there is some smearing of the pattern. This is not a surprise since there was relatively low ray coverage in that region. For smaller checkers, there is very poor resolution in the same southeast region of the array. The resolution is worse when looking at 3.50 Hz (Figure 10(c)) than when looking at 3.00 Hz (Figure 10(b)). This is likely because there are fewer acceptable ray paths through that region at higher frequencies due to attenuation. These results show that we have up to 250 m ×250 m resolution in the center of the array, and up to nearly 500 m ×500 m resolution on the fringes of the array. This level of resolution is high enough to trust the broad velocity features we find in our group velocity tomography results.

CONCLUSIONS AND FUTURE WORK

We showed that high-frequency Rayleigh waves primarily generated by traffic noise can be extracted from ambient noise recordings using cross-correlation techniques. The travel times of the fundamental-mode Rayleigh waves appear to be reliable

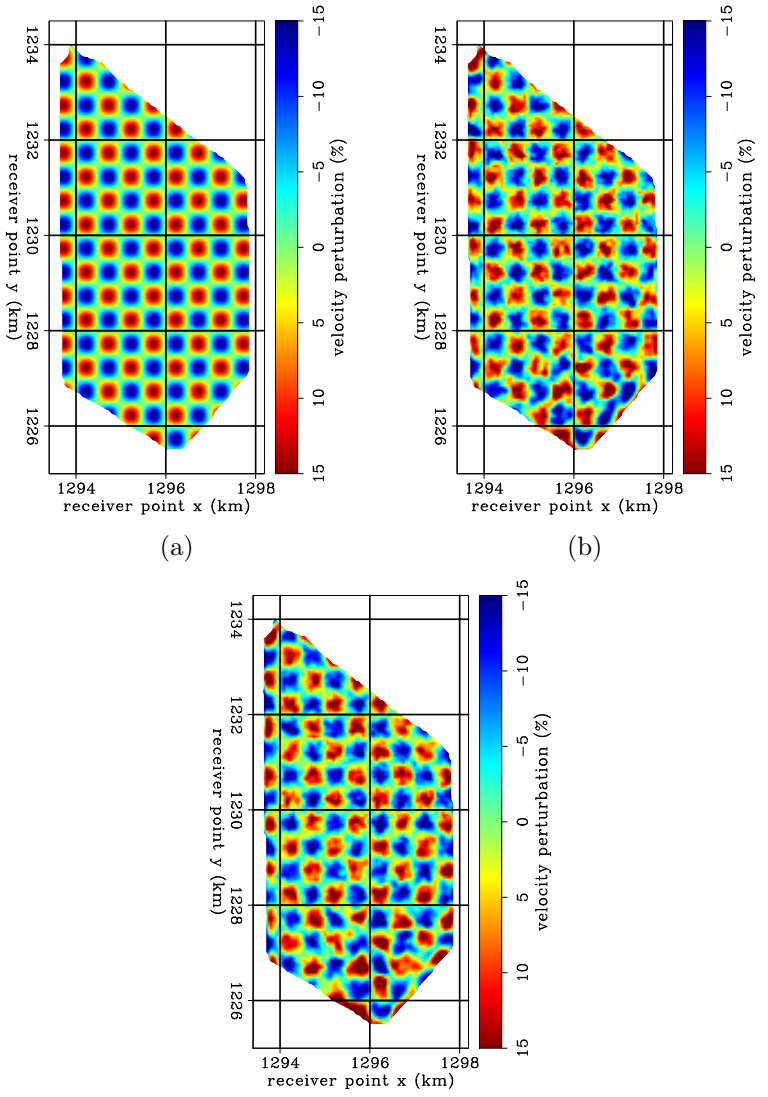

Figure 9: Checkerboard test results using sinusoidal checkers 500 m ×500 m in size and a maximum velocity perturbation of 15%. (a) Modeled checkers. (b) Inverted results at 3.00 Hz. (c) Inverted results at 3.50 Hz. Note the poor resolution in the southeast region of the array. [**CR**]

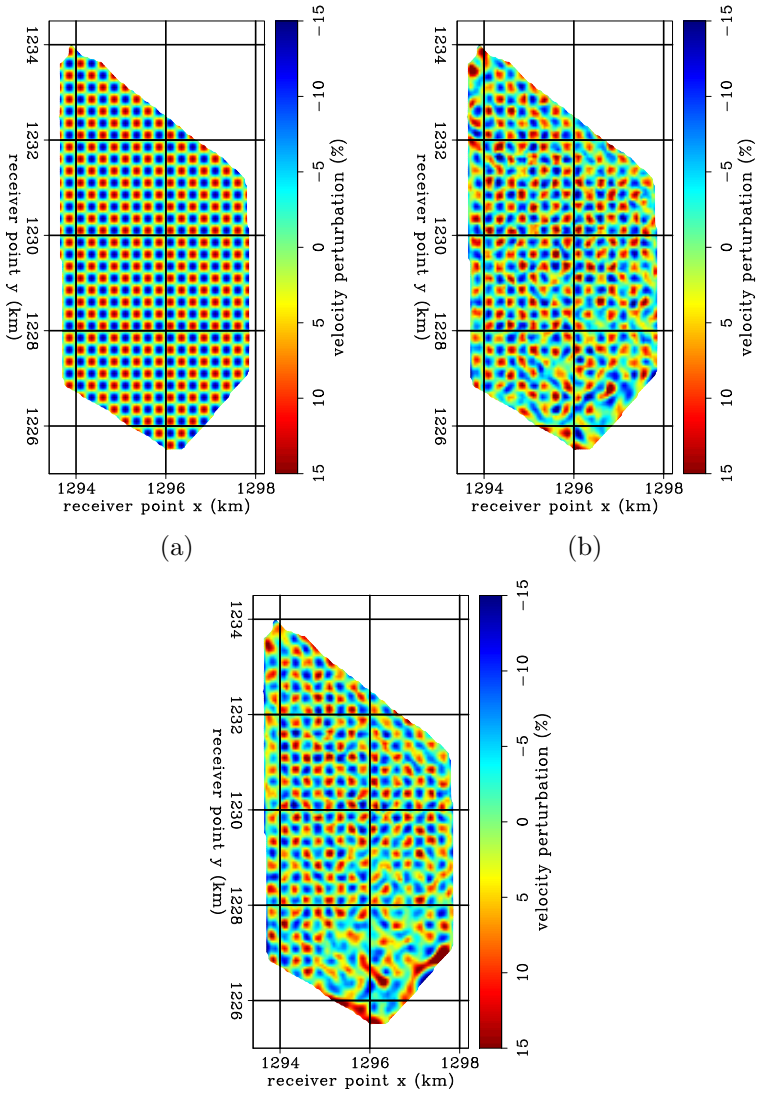

Figure 10: Checkerboard test results using sinusoidal checkers 250 m ×250 m in size and a maximum velocity perturbation of 15%. (a) Modeled checkers. (b) Inverted results at 3.00 Hz. (c) Inverted results at 3.50 Hz. Note the poor resolution in the southeast region of the array. [**CR**]

enough for performing group velocity tomography on the entire array. From our group velocity maps, we are able to distinguish velocity trends that agree with a geologic map of the region. Unconsolidated materials in the northern region appear to have relatively low velocities, while more consolidated materials in the southern region appear to have relatively high velocities. We are also able to resolve low-velocity material in Alamitos Bay, which is built on artificial fill, as well as a low velocity signature that aligns with the Newport-Inglewood Fault. Resolution tests indicate that we can trust these features. Because our investigation frequencies are high, and hence correspond to shallow depths, our results can potentially be useful for identifying regions that are susceptible to serious damage during earthquake-related shaking.

Our future goals are to improve the quality of our travel time picks, since they are currently noisy. A more careful selection of minimum and maximum virtual source-receiver distances could be beneficial, as we want to ensure that we avoid picking travel times when the fundamental and first-order modes interfere. We would also like to test our method of harnessing traffic noise by using a sparser subset of receivers because land arrays as dense as the Long Beach array are rare. Finally, it is highly unlikely we need 35-days worth of data to obtain stable correlations. We hope to create travel time maps from daily correlations for time-lapse monitoring purposes. Detectable changes in the subsurface could be due to earthquake events or precipitation.

ACKNOWLEDGMENTS

We thank Signal Hill Petroleum, Inc. for access to this data set and permission to publish. Thanks to Dan Hollis of NodalSeismic for his cooperation and help throughout this research. Thank you to Sjoerd de Ridder, Nori Nakata, Kevin Seats, Taylor Dahlke, Bob Clapp, and Stew Levin for helpful discussions. Many thanks to the sponsors of the Stanford Exploration Project for their financial support.

REFERENCES

Aster, R. C., B. Borchers, and C. H. Thurber, 2013, Parameter estimation and inverse problems: Academic Press.

Bensen, G., M. Ritzwoller, M. Barmin, A. Levshin, F. Lin, M. Moschetti, N. Shapiro, and Y. Yang, 2007, Processing seismic ambient noise data to obtain reliable broadband surface wave dispersion measurements: Geophysical Journal International, **169**, 1239–1260.

Bensen, G., M. Ritzwoller, and N. Shapiro, 2008, Broadband ambient noise surface wave tomography across the United States: Journal of Geophysical Research: Solid Earth, **113**, 1–21.

California Department of Conservation, 2012, Geologic compilation of Quaternary surficial deposits in Southern California: Technical report.

Chang, J. P., S. de Ridder, B. Biondi, et al., 2013, Power spectral densities and ambient noise cross-correlations at Long Beach: 83rd Annual International Meeting, SEG, Expanded Abstracts, 2196–2200.

Chang, J. P., N. Nakata, R. G. Clapp, B. Biondi, S. de Ridder, et al., 2014, High-frequency surface and body waves from ambient noise cross-correlations at Long Beach, CA: 84th Annual International Meeting, SEG, Expanded Abstracts, 2235–2239.

Dahlke, T., G. Beroza, J. Chang, S. de Ridder, et al., 2014, Stochastic variability of velocity estimates using eikonal tomography on the Long Beach data set: 84th Annual International Meeting, SEG, Expanded Abstracts, 2352–2356.

de Ridder, S., B. Biondi, and R. Clapp, 2014, Time-lapse seismic noise correlation tomography at Valhall: Geophysical Research Letters, **41**, 6116–6122.

de Ridder, S., B. Biondi, and D. Nichols, 2015, Elliptical-anisotropic eikonal phase-velocity tomography: Geophysical Research Letters, **42**, 758–764.

Lévěque, J.-J., L. Rivera, and G. Wittlinger, 1993, On the use of the checker-board test to assess the resolution of tomographic inversions: Geophysical Journal International, **115**, 313–318.

Lin, F.-C., D. Li, R. W. Clayton, and D. Hollis, 2013, High-resolution 3D shallow crustal structure in Long Beach, California: Application of ambient noise tomography on a dense seismic array: Geophysics, **78**, no. 4, Q45–Q56.

Mordret, A., N. M. Shapiro, and S. Singh, 2014, Seismic noise-based time-lapse monitoring of the Valhall overburden: Geophysical Research Letters, **41**, 4945–4952.

Moschetti, M., M. Ritzwoller, and N. Shapiro, 2007, Surface wave tomography of the western United States from ambient seismic noise: Rayleigh wave group velocity maps: Geochemistry, Geophysics, Geosystems, **8**, Q08010.

Nakata, N., J. P. Chang, J. F. Lawrence, and P. Boué, 2015, Body wave extraction and tomography at Long Beach, California, with ambient-noise interferometry: Journal of Geophysical Research: Solid Earth, **120**, 1159–1173.

Shapiro, N. M., M. Campillo, L. Stehly, and M. H. Ritzwoller, 2005, High-resolution surface-wave tomography from ambient seismic noise: Science, **307**, 1615–1618.

Wills, C. J. and W. Silva, 1998, Shear-wave velocity characteristics of geologic units in California: Earthquake Spectra, **14**, 533–556.

Yang, Y., M. H. Ritzwoller, F.-C. Lin, M. Moschetti, and N. M. Shapiro, 2008, Structure of the crust and uppermost mantle beneath the western United States revealed by ambient noise and earthquake tomography: Journal of Geophysical Research: Solid Earth, **113**, 1–9.